Reducing the Induction Footprint of Ultra-Wideband Antennas for Ground-Penetrating Radar in Dual-Modality Detectors

Wouter van Verre, *Member, IEEE*, Frank J. W. Podd, Xianyang Gao, Liam A. Marsh, *Member, IEEE*, John L. Davidson, David J. Daniels, *Life Fellow, IEEE*, and Anthony J. Peyton

***Abstract*— The combination of metal detection (MD) and ground-penetrating radar (GPR) has been successfully deployed to combat the threat from buried antipersonnel landmines. A number of issues arise from the close integration of these two sensing modalities. One issue is the proximity of the metallic GPR antennas to the MD coils, which affects the performance of the MD due to the eddy currents created within the GPR antenna structure. In this article, the effect of traditional solid bowtie antenna design on an MD is investigated, and avenues for the reduction of the eddy currents are explored. Three modifications to the solid bowtie design are proposed and evaluated. This article presents the measurements of the MD response to all four antenna designs using a magnetic induction spectroscopy sensor. It was found that the MD response to the bowtie antenna can be reduced by 91%–98% across the MD operating frequency band, without significantly altering the RF performance, such as reflection and transmission coefficient and radiation pattern.**

***Index Terms*— Bowtie antenna, dual modality, ground-penetrating radar (GPR), magnetic induction spectroscopy, metal detection (MD), multifrequency.**

I. Introduction

DUAL-MODALITY detectors, integrating metal detection (MD) with ground-penetrating radar (GPR), have been successfully deployed in minefields to aid in the detection of minimum-metal antipersonnel landmines. They have been shown to significantly reduce the false-alarm rate (FAR) compared with traditional detectors (MD) [1]–[3]. Furthermore, an alternative application for dual-modality detectors can be found in the localization and characterization of rebar in concrete [4].

In 2017, there were at least 4795 casualties caused by landmines, with just over half being caused by improvized devices, and the remainder by factory-made mines or mines of unknown type [5]. Typically, landmine detectors rely on MD, which suffers from a high FAR due to the large amount of metallic clutter in the soil. The number of clutter items reported is typically over 100 per landmine found [6].

Published results from trials using dual-modality landmine detection systems have shown a reduction in the FAR of up to 96.5% [1], [2]. However, the presence of the metallic GPR antennas inside the coils of the MD introduces an undesirable background signal in the output of that sensor. As a result, the MD has to subtract away this background signal, which adds extra complexity to the system.

Furthermore, the background signal can potentially be large enough to saturate amplifiers in the receiver signal conditioning chain. While digital balancing techniques [7], [8] can be employed to prevent saturation of the amplifiers, this adds to the complexity of the system, increasing cost, and power consumption and could potentially introduce extra noise into the receiver signal processing chain. It is therefore preferable to mitigate the root cause of the issue, by reducing the MD response to the GPR antennas. In this article, the magnitude of the MD signal caused by the GPR antennas will also be referred to as the "induction footprint."

Commercial GPR systems commonly use bowtie antennas [9], although other designs such as spiral antennas are also used [3]. The GPR system under development at The University of Manchester (Fig. 1) also uses bowtie antennas [8].

In this article, which extends a previous conference publication [10], the effect of bowtie antennas in dual-modality landmine detection systems will be considered. The results are presented based on an analytical model, simulations using CST Microwave Studio and measurements. Three new modifications to the traditional solid bowtie design are proposed and evaluated in this article. Novel measurements of the spectroscopic response of each of the antenna designs are also reported. These measurements will be of particular interest to future designers of dual-modality MD and GPR detectors.

II. Background

When a pulse is injected into a bowtie antenna, the current travels mostly along the edges of the antenna elements [11],

Manuscript received April 2, 2020; revised July 14, 2020; accepted August 3, 2020. Date of publication October 5, 2020; date of current version March 3, 2021. This work was supported in part by The Sir Bobby Charlton Foundation and in part by Engineering and Physical Sciences Research Council (EPSRC) under Grant EP/N509565/1. *(Corresponding author: Wouter van Verre.)*

The authors are with the Department of Electrical and Electronic Engineering, The University of Manchester, Manchester M13 9PL, U.K. (e-mail: wouter.vanverre@manchester.ac.uk).

Color versions of one or more of the figures in this article are available online at https://ieeexplore.ieee.org.

Digital Object Identifier 10.1109/TAP.2020.3026909

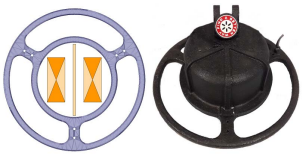

Fig. 1. Photograph of a typical dual-modality detector and an image of the placement of the GPR antennas.

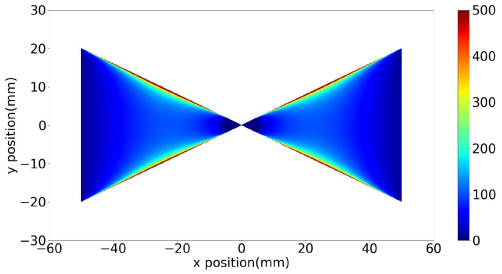

Fig. 2. Current distribution on bowtie antenna according to (3) at $t = 0.1$ ns.

while the current density at the center of the antennas is much lower. This suggests that it may be possible to remove metal from the center of a bowtie antenna, without adversely affecting the RF characteristics, such as the shape of the radiated pulse and the radiation pattern.

Compton *et al.* [12] developed an analytical model for the current distribution of the bowtie antenna. From this model, it can be seen that the current distribution of the feed current on the bowtie follows the following behavior, which is expressed in polar coordinates:

$$\frac{1}{\sqrt{\cos^2\phi - \cos^2\phi_0}} \tag{1}$$

where ϕ_0 is half the bowtie flare angle. This agrees with the previous observation that the current travels mainly along the edge of the antenna.

Muslim *et al.* [13] investigated some of the properties of a hollow bowtie antenna. Their work showed that, in general, this shape is still a functional antenna similar to the solid bowtie. However, the aim of the work was to improve a specific resonance, so it is not clear from this work if the metal can be removed in such a way that the ultrawideband (UWB) radiation characteristics do not change.

Andre and Khayam [14] reduced the surface area of the bowtie antenna by removing a circular cut from the far edge of each bowtie element. Their choice on which area of the bowtie antenna to remove was also guided by the current density distribution, in this case at one specific frequency. This work demonstrates that bowtie antennas with a gap in the center still behave in a similar manner to solid bowtie designs. However, this work also set out to reduce the return loss at a specific frequency, so it is not yet clear if metal can be removed in such a way that the radiated pulse does not get changed significantly.

The previously mentioned works did not consider GPR applications and have therefore not evaluated certain key properties for that use case. In particular, the time-domain signal in both free space and over a dielectric, as well as the radiation pattern of the antennas, was not evaluated.

Wire bowtie antennas are also interesting in this context. The wire bowtie replaces the solid sheet of metal with metallic wires or fingers, arranged such that they have the same outline as the solid bowtie antenna. It is expected that such an antenna would have a small induction footprint, as there are no large loops in which the induced currents can flow.

Lestari *et al.* [15], [16] investigated the unloaded wire bowtie antenna for GPR applications, investigating the effects of flare angle and soil. Further research was done on loaded wire bowtie antennas in [17]–[20]. Unfortunately, these papers do not provide direct comparisons between the wire bowtie antenna and the equivalent solid bowtie antenna.

The aim of this article is to reduce the induction footprint of the GPR bowtie antenna while keeping the antenna response as close as possible to that of the solid bowtie antenna. The proposed solution is to leave only the edges of the bowtie antenna, based on the observation that this is where the surface current density is highest.

III. Analytical Solution

Compton *et al.* [12] described a full solution for the current distribution on an infinitesimally thin bowtie antenna. They first describe a simple single-current model, which does not consider the effects of the finite length of the bowtie. However, this model can still be used for the outgoing wave due to the current at the feed. This corresponds to times $t < \tau$ where $\tau = L/c$, the time it takes for the current pulse to travel the length of the bowtie antenna. The single-current model is given by the following equation [12]:

$$\mathbf{J} = \frac{\pm e^{-\gamma r}/r}{\sqrt{\cos^2\phi - \cos^2\phi_0}}\hat{\mathbf{r}} \tag{2}$$

where the $e^{-\gamma r}/r$ term describes an outwards traveling current wave, and the propagation constant γ can be written as $\gamma = \alpha + j\beta$, with α representing the reduction in current amplitude due to radiation [12]. For the simplest model of a bowtie antenna in free space, without a dielectric β can be estimated as $\beta = (\omega/c)$, where c is the speed of light in a vacuum. ϕ_0 corresponds to half of the bowtie flare angle. Furthermore, there is an implicit $e^{j\omega t}$ time dependence.

Therefore, the current distribution at time t, at a point (ϕ, r), due to a set of frequencies F, can be determined as follows:

$$\mathbf{J}(\phi, r, t) = \sum_{f\in F} \Re\left[\frac{\pm e^{-\gamma r}/r}{\sqrt{\cos^2\phi - \cos^2\phi_0}} e^{j\omega t}\right]\hat{\mathbf{r}}. \tag{3}$$

Fig. 2 shows the current distribution on a bowtie calculated using (3). The bowtie antenna has elements of length 50 mm and width 40 mm so that the flare angle is $43.6°(\phi_0 = 21.8°)$. The set of frequencies contains 6001 points, evenly spaced between 0 and 6 GHz. The surface current was evaluated at $t = 0.1$ ns.

IV. Experimental Methodology

In this article, four antenna designs are evaluated for their suitability to dual-modality detectors. The aim is to modify the traditional bowtie antenna, commonly employed in

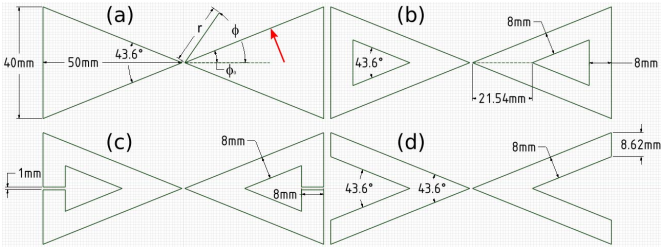

Fig. 3. Drawings of the four antenna designs. (a)–(d) Solid, Hollow, Hollow + Slot, and Chevron, respectively.

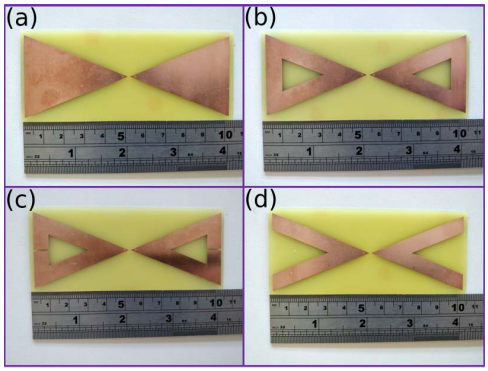

Fig. 4. Photograph of the four antennas under test. (a)–(d) Solid, Hollow, Hollow + Slot, and Chevron, respectively.

GPR systems, such that the induced voltage on the receive coil of a spectroscopy-based metal detector is reduced.

The four antennas' designs, which increasingly reduce the amount of copper and the maximum loop size of the eddy currents, are shown in Figs. 3 and 4. The first antenna design is a traditional solid bowtie antenna, with each element of the antenna measuring 50 mm long and 40 mm wide (flare angle 43.6°). The next design shows the same design, with the central copper removed, leaving behind limbs with a width of 8 mm. The third design iterates on the hollow bowtie design by placing a small slot on the far side of the antennas. This cut reduces the maximum loop area for any eddy currents on the antenna surface. The final antenna prototype removes the entire vertical limb on the far side of the antenna, leaving a "chevron" shape, also with a limb width of 8 mm.

CST Microwave Studio was used to estimate the RF performance of the proposed antenna designs. In these simulations, the bowtie length was 50 mm with a flare angle of 43.6° unless otherwise noted. The port impedance in the simulations was fixed at 200 Ω, and the excitation was the default 6 GHz Gaussian pulse (full-width at half-maximum = 0.135 ns).

A Copper Mountain S5065 vector network analyzer (VNA) was used to evaluate the performance of the antennas, measuring parameters including the reflection and transmission coefficient and the radiation pattern, in free space A transformer balun, using the Mini-Circuits TCM4-452X+, shown in Fig. 5, was used to connect the VNA to the antennas during these tests. The layout of the balun board follows the Mini-Circuits recommended layout, where the balanced signals are on 50 Ω traces. The VNA frequency sweep was

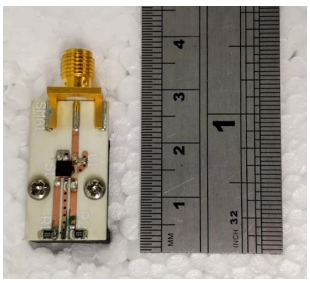

Fig. 5. Photograph of the balun used in this experiment.

configured for 10 MHz–6 GHz in 600 steps (10 MHz step frequency). A Kaiser window ($\beta = 12$) was used in the inversion to the time domain.

The radiation patterns in the E- and H-planes of each antenna were measured inside an anechoic chamber by placing one antenna on a turntable with one rotating axis, with the second antenna mounted on a fixed tripod. The mounting angle of the antennas with respect to the turntable was varied to measure the radiation pattern in different planes.

Further tests were undertaken to measure the performance of the antenna prototypes when placed over soil. Computer simulations were performed with the antennas over a dielectric half-space ($\epsilon_r = 9$), with a 6 cm diameter PEC sphere buried at a depth of 5 cm. In the laboratory tests, a metallic sphere (6 cm diameter) was buried in a box of soil (measuring $70 \times 45 \times 30$ cm), and the antennas were mounted side-by-side over the soil, using polystyrene foam as a spacer. The sphere was chosen because its RCS value is aspect independent and it can be calculated theoretically (-25.5 dBsm for this sphere). In this experiment, the transformer baluns were replaced by a pair of tapered microstrip baluns, whose design was modified from that presented by Vinayagamoorthy *et al.* [21].

The transformer baluns are smaller, have a lower reflection coefficient, and have better reproducibility between devices, but their output impedance is lower than that of the tapered baluns, which were designed to have a 200 Ω output impedance. In previous work, it has been found [22], [23] that feed impedance at the antenna terminals changes the time-domain signal of the radiated pulse. The higher output impedance from the tapered baluns is preferred in this experiment to reduce the ringing in the time domain.

Finally, the induction footprint of the different antenna designs is evaluated using the MIS sensor, which forms part of a prototype dual-modality landmine detector. The hardware for this prototype has been described in [8], and the placement of the antennas inside the coils is shown in Fig. 1. The calibration procedure described in [8] was used in this experiment as well. Using the MIS hardware, the response of the antennas, relative to the ferrite test piece used for calibration, was evaluated simultaneously at five frequencies between 10 and 50 kHz.

The peak-to-peak voltage of the transmitter waveform was reduced such that the receiver electronics did not saturate. For multifrequency spectroscopic MD, it is hard to calculate a transimpedance value at which the detector is saturated. The saturation point is highly dependent on the properties of the transmitted waveform, such as the number and the

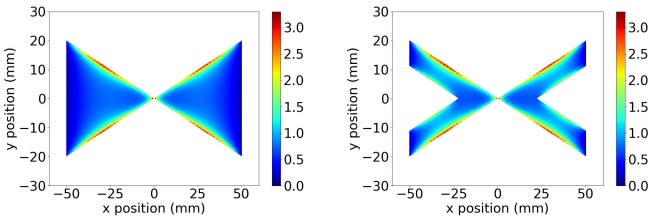

Fig. 6. Simulated surface currents. (a) Solid bowtie. (b) Chevron bowtie.

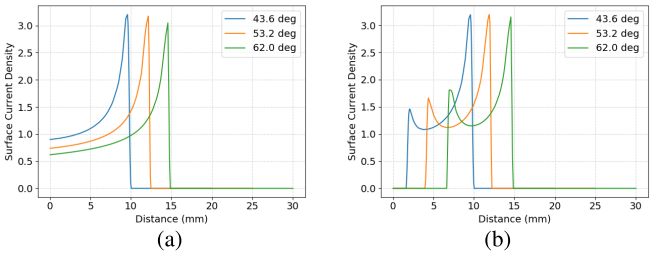

Fig. 7. Surface current profile from simulations of bowties with varying flare angles. (a) Solid bowtie. (b) Chevron bowtie.

specific harmonics that are excited, their relative magnitudes and phases, and the waveform peak-to-peak voltage. Even for a given transmit waveform, the limit would still be dependent on object properties, as different objects will cause different phase shifts between the transmitter and receiver waveforms, which can lead to constructive and destructive interference. Therefore, the firmware in the metal detector monitors both ADC channels and provides a warning to the operator if saturation is detected. This warning was used to select a value for the peak-to-peak voltage of the transmit waveform, which avoids saturation for all the antennas under investigation.

V. Simulated Results

A. Surface Currents

Using computer simulations, the surface currents on the bowtie antenna can be evaluated. Fig. 6 shows the distribution of the surface current after exciting the antenna with a Gaussian pulse. This figure shows current after approximately 0.4 ns of simulated time. Fig. 6(a) shows agreement between the simulation and the analytical result in Fig. 2.

It is also possible to evaluate the surface current profile along a specified path and repeat this for different flare angles and different antenna designs. The path chosen here runs perpendicular to the antenna edge, starting at $y = 0$ cm and crossing the antenna edge at the point where $\mathbf{J}$ is at its maximum. This path is indicated with an arrow in Fig. 2(a). Fig. 7(a) shows how the current along the path varies with the flare angle of a solid bowtie antenna. Similarly, Fig. 7(b) shows the same for the chevron design.

Figs. 6 and 7 show a concentration of current on the outside edge of the bowtie antenna. Furthermore, in the case of the chevron design, a concentration of current on the inside edge can be observed. The general shape of the surface current profiles does not change with the bowtie flare angle. Finally, it can be seen that the current distribution near the outer edge remains the same for both the solid and chevron design, suggesting that the removal of copper does not have an effect on this current pulse.

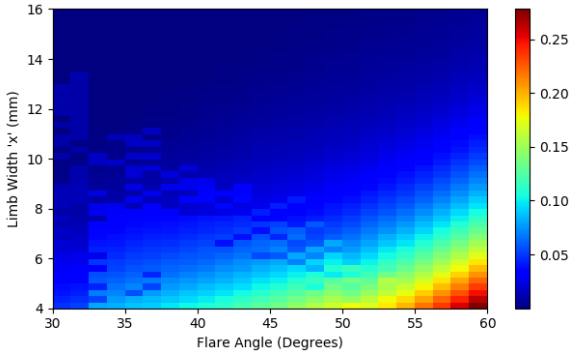

Fig. 8. MSE as a function of flare angle and limb width.

B. Minimum Limb Width

Simulations were performed to determine the minimum width of the antenna limbs required to maintain good RF performance. As has been discussed previously, the minimum width may also depend on the flare angle of the bowtie antennas. For these simulations, the width of the limbs and the flare angle of the "chevron" antenna design were varied. The corresponding simulations were also performed for the solid bowtie design.

The aim of this work is to minimize the changes to the RF radiation characteristics, particularly to the time-domain signals, while reducing the induction footprint of the antennas. The exact shape of the pulse, and its optimization, will be considered in future work. The performance of the designs was evaluated by calculating the root mean square of the difference between the received time-domain signals for the chevron designs compared with the solid bowtie design. This metric will be referred to as the mean square error (mse)

$$mse = \sqrt{\frac{1}{N}\sum_{n=0}^{N-1}(x_s[n] - x_c[n])^2} \tag{4}$$

where x_s and x_c are both time-domain signals of length N, corresponding to the solid and chevron bowtie cases, respectively.

The resulting mse values as a function of flare angle and limb width are shown in Fig. 8. It can be seen that the minimum width at which a given level of mse can be achieved is dependent on the flare angle of the antenna. Based on these results, a limb width of 8 mm was chosen for the antenna designs in this article, which have a flare angle of 43.6°.

C. Free Space

In all the following simulations, the flare angle of the bowtie is 43.6° and, where relevant, the limb width was 8 mm. The antennas were placed face-to-face down the boresight, with a separation of 30 cm.

The simulated reflection and transmission coefficients for all four antenna designs are shown in Fig. 9(a) and (b), respectively. It can be seen that the results up to 3 GHz match to within 0.75 dB for S_{11} and 1.8 dB for S_{21}.

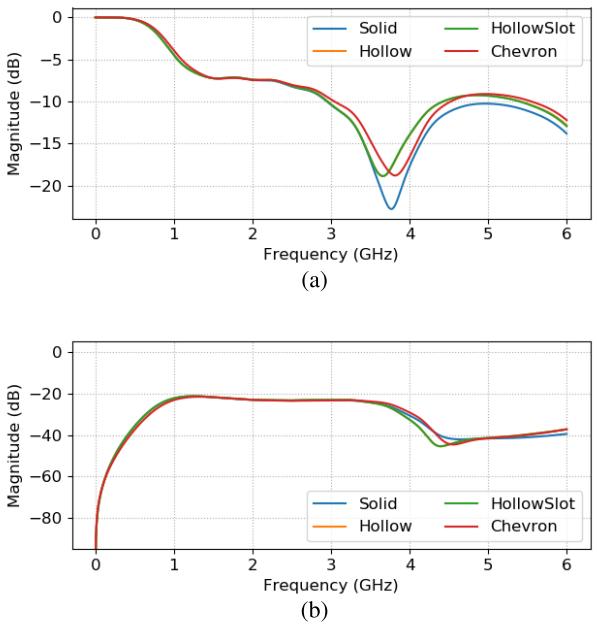

Fig. 9. Antenna coefficients from simulations. (a) Reflection coefficients. (b) Transmission coefficients.

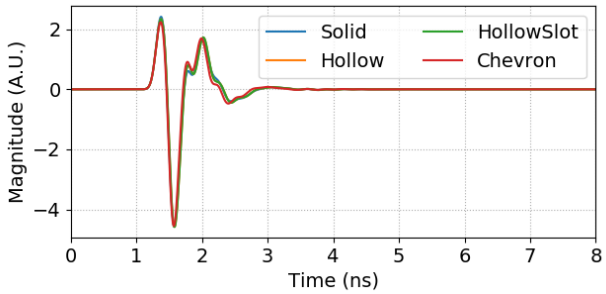

Fig. 10. Time-domain signals from simulations.

The time-domain signal of the pulse transmitted between the two antennas (see Fig. 10) also remains largely unchanged, with the maximum deviation being less than 6.8% of the peak-to-peak magnitude.

D. Radiation Pattern

The far-field radiation patterns of the four antenna designs were also evaluated using computer simulations. In Fig. 11, the E- and H-plane patterns are shown at three frequencies in the operating band of the bowtie antenna. The radiation patterns are identical (to within 0.75 dB) for all four antenna designs under consideration.

E. Buried Object Detection

In GPR applications, it is important that the antennas are able to transmit sufficient energy into the ground to lead to a positive detection of buried targets. As described in Section IV, a simulation of the antennas over a dielectric half-space ($\epsilon_r = 9$) with a buried PEC sphere was used to validate the ability of the antenna designs to transmit energy into the ground. The two designs simulated in this section were

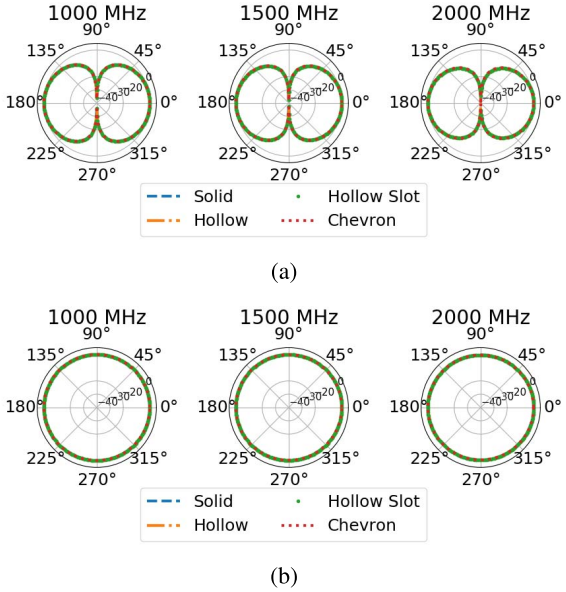

Fig. 11. Simulated radiation pattern of the antennas under consideration. (a) E-plane. (b) H-plane.

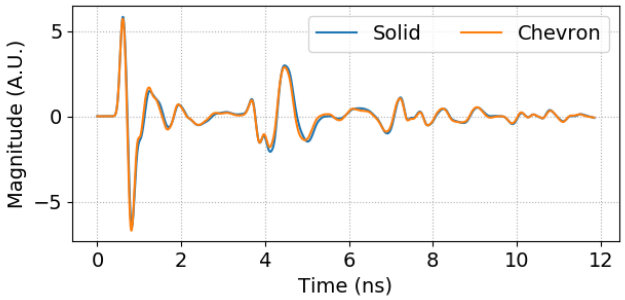

Fig. 12. Simulated response of the antennas over a dielectric half-space with a buried PEC sphere.

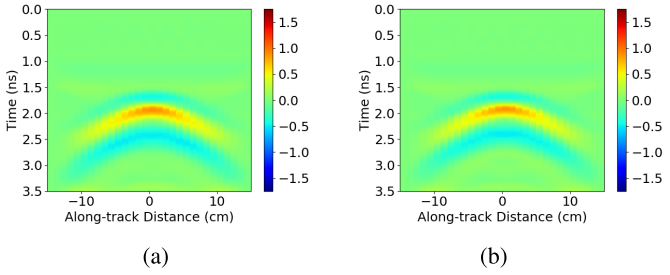

Fig. 13. Simulated B-scan over metal sphere. (a) Using solid bowties. (b) Using chevron bowties.

the solid and chevron bowtie antennas. Background removal was applied to the B-scans to highlight the response due to the buried sphere.

Figs. 12 and 13 show the simulated A-scan and B-scan results, respectively. The difference between the two results is less than 5.8% of the peak-to-peak value of the waveform, demonstrating that the reduction in copper surface area between the solid chevron antenna design does not lead to a significant reduction in energy coupling into the dielectric material. The B-scans also show that the radiation at angles

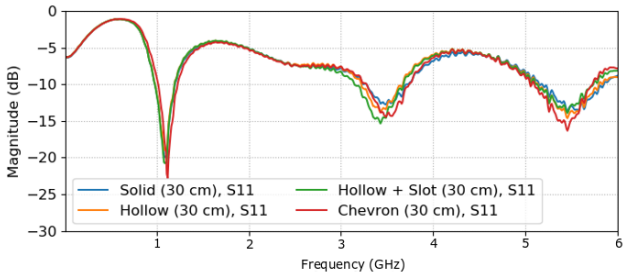

Fig. 14. S11 measurements of the different antenna designs.

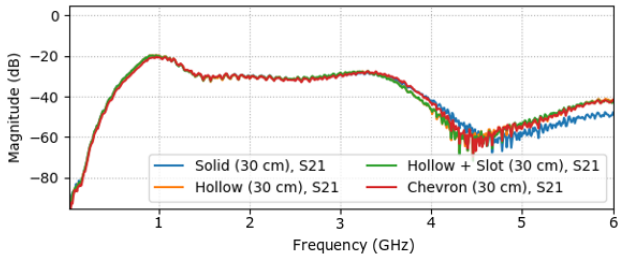

Fig. 15. S21 measurements of the different antenna designs.

other than down the boresight also does not differ significantly between both designs.

VI. Experimental Results

A. Free-Space Measurements

Fig. 14 shows the reflection coefficients of the antenna designs under test. This test evaluates the antenna and balun combination in free space. It can be seen that each successive step of removing copper from the antennas does not significantly impact the reflection coefficient of the antennas, which varies by less than 4.8 dB up to 3 GHz. The biggest variation occurs at the resonance of the frequency, and the variation outside of the resonance is smaller.

The transmission coefficient, shown in Fig. 15 of the antennas in a face-to-face configuration, up to 3 GHz, is also not significantly different (to within 1.6 dB) between the four antenna designs. There is a larger difference in the transmission coefficient after approximately 4 GHz, between the solid bowtie and all other designs. However, as can be seen from the same figure, this falls outside the working band of the antennas.

The transmission in the time domain is also an important consideration for antenna used in GPR applications. The time-domain signal from the face-to-face test is shown in Fig. 16. The difference between the four waveforms is less than 8.5% of the peak-to-peak magnitude.

B. Radiation Pattern

The radiation patterns of the prototype antennas were measured, as described in Section IV. The results at three frequencies (1000, 1500, and 2000 MHz) have been included in Fig. 17.

The three designs evaluated with this setup show the same patterns, in both the E- and H-plane. The measured radiation

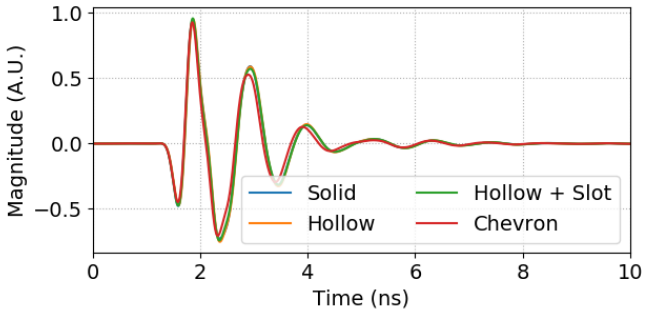

Fig. 16. Time-domain signal of the different antenna designs.

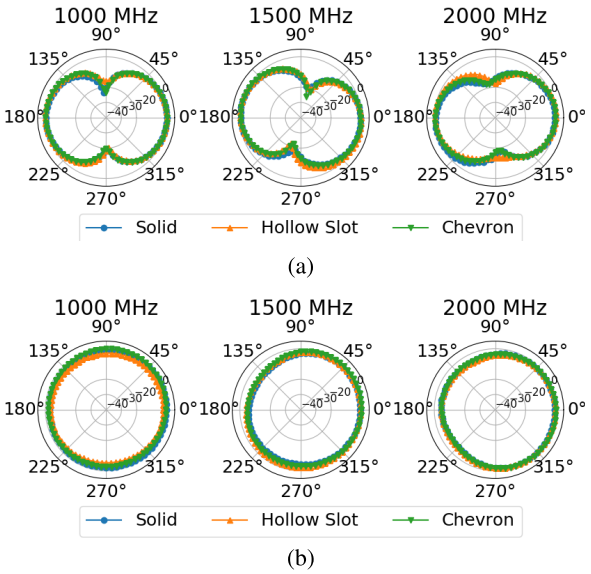

Fig. 17. Measured radiation pattern of the antenna prototypes. (a) E-plane. (b) H-plane.

patterns are in agreement with those presented in Fig. 11, which were derived from simulations. Some amount of skewing of the pattern can be observed in the E-plane, which is likely due to the variability in the mounting of the antennas on the test stand. The feed cables and baluns can also cause skew in the radiation patterns [24]. The variation between the different antenna designs falls within the measurement error.

C. Buried Object Detection

Fig. 18 shows the A-scans taken directly above the buried metal sphere. This figure shows that the solid bowtie antenna and the chevron bowtie design give the same response to buried targets, to be within 6.3% of the peak-to-peak value of the waveform. The difference between the two B-scans, which are shown in Fig. 19, is within 10%.

The only processing applied to the B-scan images is background subtraction. There is a small surface reflection at the end of the B-scan images. Since it is observed with both antenna designs, this is likely a feature of the test setup, such as inhomogeneity of the soil moisture content or an environmental clutter source.

VII. MIS System Response

The reduction in MIS system response due to the changes in the antenna shape has been characterized using a spectroscopic

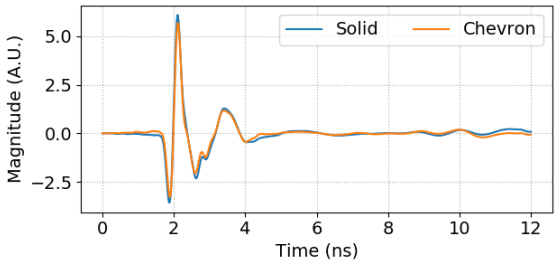

Fig. 18. Measured signal over buried metal sphere.

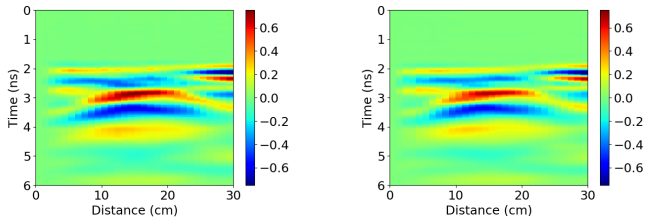

Fig. 19. Measured B-scans over metal sphere. (a) Using solid bowties. (b) Using chevron bowties.

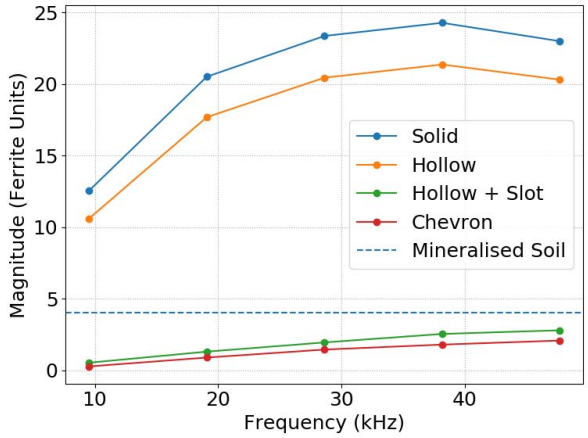

Fig. 20. Magnitude of the MIS system response.

MIS sensor prototype. In this experiment, a pair of antennas of each shape was placed inside the MIS receiver coils, as shown in Fig. 1. The magnitude of the response is shown in Fig. 20. It was found that the receiver electronics would saturate unless the transmitter current for the MIS sensor was reduced to 40% of the maximum.

The response to these antennas can be compared to that of mineralised soil and various metal objects tested in previous work [25]. A heavily mineralized soil, at a typical stand-off distance of 2–3 cm, has a response with a magnitude of approximately four ferrite units (indicated with the dashed line in Fig. 20). A PMA-2 landmine, at a distance of 7.5 cm has a peak magnitude of less than 0.02 ferrite units, for comparison. The dynamic range for the MIS system is chosen such that the mineralized soil does not saturate the electronics while also being able to detect buried minimum-metal landmines. The solid bowtie antenna has a response that is 5–6 larger than that of the mineralized soil, which puts it outside the sensor's dynamic range.

From these figures, it can be seen that removing the central copper from the solid bowtie antenna reduces the MIS sensor response by approximately 10%. However, the most significant change occurs when placing a slot in the far limb of the hollowed-out bowtie antenna. At this point, the large eddy current loop around the edges of the bowtie antenna is broken, significantly reducing the magnitude of the MIS response. A further reduction in magnitude takes place when the far limb is removed entirely, resulting the "chevron" shape antenna. The reduction in the magnitude of the response between the solid bowtie design and the chevron design is 98% at the lowest frequency and 91% at the highest frequency.

VIII. Conclusion

When designing dual-modality detection systems employing both MIS and GPR, it is important to consider the impact of the metallic GPR components on the metal detector. The presence of the GPR antennas can interfere with the balance between the metal detector coils, which have been carefully designed to minimize the net-induced voltage on the receive coil, under normal background operating conditions. This can lead to a reduction in the available dynamic range or even saturation of the receive amplifiers.

Therefore, four variants of the bowtie antenna design have been evaluated to improve the compatibility of GPR antennas with spectroscopic MD systems. Starting from the traditional solid bowtie antenna, the successive designs gradually reduce the metal content of the antennas. The maximum loop size in which the induced eddy currents can flow is also reduced.

It has been shown that based on knowledge of the current flow on bowtie antennas, it is possible to reduce the induction footprint of these antennas without significantly altering their radiation characteristics. The changes in radiation characteristics for the proposed antenna designs have been investigated using simulation in and have been verified using real-world measurements.

In this article, the reflection coefficient, transmission coefficient, and time-domain transmission signal have been characterized in free space and shown to be consistent across all four designs. The radiation patterns of the designs have also been measured using a turntable and found to be consistent. Another important characteristic of GPR antennas is their performance when placed over a dielectric material such as soil. Therefore, another experiment was performed, measuring the response of the bowtie antennas over a box of soil containing a metallic sphere. Here, too there was good agreement between the antenna designs.

Measurements were also taken using a prototype MIS sensor to verify the reduction in the induction footprint of the proposed antenna designs. It was found that a pair of solid bowtie antennas saturate the receiver electronics, illustrating the nature of the problem with placing GPR antennas in close proximity to the coils of MIS sensors, particularly when they are placed in a region of high sensitivity of the coils.

It has been shown that a significant ($>10\%$) reduction in induction footprint for GPR antennas requires a reduction in the maximum loop area of the eddy currents. The experiments

have also shown that the proposed "chevron" bowtie design reduces the magnitude of the MIS response by 91%–98%, over the range of operating frequencies.

Opportunities for further investigations into improving MIS and GPR compatibility have also been identified. The development of either a model-based or empirical understanding of the induction footprint of a particular GPR antenna design is desirable so that designers of dual-modality equipment can make predictions on this compatibility issue.

Second, the presence of the GPR antennas may lead to changes in the sensitivity map of the MIS sensor. Therefore, further work could measure the sensitivity map of the MIS sensor and the effects of GPR antennas on this. Finally, the effects of the MIS coils on the radiation characteristics of the GPR antennas should also be investigated.

ACKNOWLEDGMENT

This work was conducted as part of the program "SEMIS III" (Scanning electromagnetic mine inspection system).

REFERENCES

[1] D. Daniels, J. Braustein, and M. Nevard, "Using MINEHOUND in cambodia and Afghanistan," *J. Erw Mine Action*, vol. 18, no. 2, p. 14, 2014.

[2] The Halo Trust. (2001). *Halo Utilises Dual-Sensor Detector | The Halo Trust*. [Online]. Available: https://www.halotrust.org/media-centre/news/halo-utilises-dual-sensor-d%etector/

[3] M. Sato, K. Kikuta, and I. Chernyak, "Dual sensor, 'ALIS for humanitarian demining," in *Proc. 17th Int. Conf. Ground Penetrating Radar*, Jun. 2018, pp. 1–4.

[4] F. Zhou, Z. Chen, H. Liu, J. Cui, B. Spencer, and G. Fang, "Simultaneous estimation of rebar diameter and cover thickness by a GPR-EMI dual sensor," *Sensors*, vol. 18, no. 9, p. 2969, Sep. 2018.

[5] ICBL. (2018). *Landmine Monitor 2018*. [Online]. Available: www.the-monitor.org/cp

[6] D. J. Daniels, "A review of GPR for landmine detection," *Sens. Imag., Int. J.*, vol. 7, no. 3, pp. 90–123, Sep. 2006.

[7] D. Ambrus, D. Vasic, and V. Bilas, "Automatic compensation of primary field coupling for a frequency-domain electromagnetic induction sensor," in *Proc. IEEE Int. Instrum. Meas. Technol. Conf. (I2MTC)*, May 2017, pp. 1–5.

[8] L. A. Marsh *et al.*, "Combining electromagnetic spectroscopy and ground-penetrating radar for the detection of anti-personnel landmines," *Sensors*, vol. 19, no. 15, p. 3390, Aug. 2019.

[9] C. Warren and A. Giannopoulos, "Creating finite-difference time-domain models of commercial ground-penetrating radar antennas using Taguchi's optimization method," *Geophysics*, vol. 76, no. 2, pp. G37–G47, Mar. 2011.

[10] W. van Verre, X. Gao, F. J. Podd, D. J. Daniels, and A. J. Peyton, "GPR bowtie antennas with reduced induction footprints for dual-modality detectors," in *Proc. IEEE Int. Symp. Antennas Propag. USNC-URSI Radio Sci. Meeting*, Jul. 2019, pp. 600–859.

[11] C. J. Leat, N. V. Shuley, and G. F. Stickley, "Triangular-patch model of bowtie antennas: Validation against brown and woodward," *IEE Proc. Microw., Antennas Propag.*, vol. 145, no. 6, p. 465, Dec. 1998.

[12] R. Compton, R. McPhedran, Z. Popovic, G. Rebeiz, P. Tong, and D. Rutledge, "Bow-tie antennas on a dielectric half-space: Theory and experiment," *IEEE Trans. Antennas Propag.*, vol. 35, no. 6, pp. 622–631, Jun. 1987.

[13] J. Muslim *et al.*, "Improvement of bowtie UHF antenna model for detecting PD in GIS," *Procedia Technol.*, vol. 11, pp. 227–234, Jan. 2013.

[14] H. Andre and U. Khayam, "Design of new shape printed bowtie antena for ultra high frequency partial discharge sensor in gas-insulated substations," in *Proc. Int. Conf. Inf. Technol. Electr. Eng. (ICITEE)*, Oct. 2013, pp. 355–359.

[15] A. A. Lestari, A. G. Yarovoy, and L. P. Ligthart, "Numerical and experimental analysis of circular-end wire bow-tie antennas over a lossy ground," *IEEE Trans. Antennas Propag.*, vol. 52, no. 1, pp. 26–35, Jan. 2004.

[16] A. A. Lestari, A. G. Yarovoy, and L. P. Ligthart, "Adaptive wire bow-tie antenna for GPR applications," *IEEE Trans. Antennas Propag.*, vol. 53, no. 5, pp. 1745–1754, May 2005.

[17] A. A. Lestari, E. Bharata, A. B. Suksmono, A. Kurniawan, A. G. Yarovoy, and L. P. Ligthart, "A modified bow-tie antenna for improved pulse radiation," *IEEE Trans. Antennas Propag.*, vol. 58, no. 7, pp. 2184–2192, Jul. 2010.

[18] A. R. Bretones, C. Moreno de Jong van Coevorden, M. F. Pantoja, F. Garcia Ruiz, S. G. Garcia, and R. Gomez Martin, "GA design of broadband thin-wire antennas for GPR applications," in *Proc. 3rd Int. Workshop Adv. Ground Penetrating Radar, IWAGPR*, May 2005, pp. 143–146.

[19] S. W. Chung, R. A. Abd-Alhameed, C. H. See, and P. S. Excell, "Wideband loaded wire bow-tie antenna for near field imaging using genetic algorithms," in *Proc. Prog. Electromagn. Res. Symp.*, no. 1, 2008, pp. 308–312.

[20] C. H. See, R. A. Abd-Alhameed, S. W. J. Chung, D. Zhou, H. Al-Ahmad, and P. S. Excell, "The design of a resistively loaded bowtie antenna for applications in breast cancer detection systems," *IEEE Trans. Antennas Propag.*, vol. 60, no. 5, pp. 2526–2530, May 2012.

[21] K. Vinayagamoorthy, J. Coetzee, and D. Jayalath, "Microstrip to parallel strip balun as spiral antenna feed," in *Proc. IEEE 75th Veh. Technol. Conf. (VTC Spring)*, May 2012, pp. 1–5.

[22] X. Gao, F. J. Podd, W. van Verre, D. J. Daniels, Y. M. Tan, and A. J. Peyton, "Simulation of ground penetrating radar for anti-personnel landmine detection," in *Proc. 17th Int. Conf. Ground Penetrating Radar (GPR)*, Jun. 2018, pp. 1–4.

[23] X. Gao, F. J. W. Podd, W. Van Verre, D. J. Daniels, and A. J. Peyton, "Investigating the performance of bi-static GPR antennas for near-surface object detection," *Sensors*, vol. 19, no. 1, p. 170, Jan. 2019.

[24] T. Fukasawa, N. Yoneda, and H. Miyashita, "Investigation on current reduction effects of baluns for measurement of a small antenna," *IEEE Trans. Antennas Propag.*, vol. 67, no. 7, pp. 4323–4329, Jul. 2019.

[25] W. van Verre, L. A. Marsh, J. L. Davidson, E. Cheadle, F. J. W. Podd, and A. J. Peyton, "Detection of metallic objects in mineralized soil using magnetic induction spectroscopy," *IEEE Trans. Geosci. Remote Sens.*, early access, Jun. 9, 2020, doi: 10.1109/TGRS.2020.2994814.

Wouter van Verre (Member, IEEE) received the B.Eng. degree (Hons.) in electrical and electronics engineering from The University of Manchester, Manchester, U.K., in 2016, where he is currently pursuing the Ph.D. degree in the use of electromagnetic methods for the detection of buried landmines.

His other research interests include the use of metal detection in polar environments and MIMO ground-penetrating radar.

Frank J. W. Podd was born in Lowestoft, U.K., in 1970. He received the B.Sc. degree in theoretical physics, the M.Sc. degree in pattern recognition and machine learning, and the Ph.D. degree in medical image processing from the University of Surrey, Guildford, U.K., in 1992, 1993, and 1997, respectively.

He has worked in academia and industry, creating scientific instruments, and now teaches embedded systems at The University of Manchester, Manchester, U.K. His current research interest is in MIMO ground-penetrating radar.

Xianyang Gao was born in Liaoning, China, in June 1990. He received the bachelor's degree in control science and engineering and the master's degree in automation from Shandong University, Jinan, China, in 2013 and 2016, respectively.

His previous works include fieldbus control systems and distributed control systems. In 2016, he joined The University of Manchester, Manchester, U.K., as a Ph.D. Researcher under the Scanning Electromagnetic Inspection System (SEMIS) research program. His Ph.D. study is funded by the CSC-UoM joint scholarship and the SEMIS research is funded by the Sir Bobby Charlton Foundation. He works on advanced electromagnetic methods for humanitarian demining. His main research interests are in ultrawideband antennas and the ground-penetrating radar system.

Liam A. Marsh (Member, IEEE) received the M.Eng. degree (Hons.) in electrical engineering and electronics from the Institute of Science and Technology, The University of Manchester, Manchester, U.K., in 2007, and the Ph.D. degree in electromagnetic tomography and people screening from The University of Manchester in 2011.

He subsequently joined the Sensing, Imaging and Signal Processing Research Group, School of Electrical and Electronic Engineering, The University of Manchester, as a Research Associate. In 2018, he was appointed as a Lecturer in embedded systems at The University of Manchester. His current research interests include the development of electromagnetic sensor systems for security, landmine detection, and polar sensing.

John L. Davidson received the B.Sc. degree (Hons.) in engineering physics and the Ph.D. degree in Mössbauer spectroscopy from Sheffield Hallam University (SHU), Sheffield, U.K., in 1993 and 1997, respectively.

As a Research Fellow at the University of Southampton, Southampton, U.K., from 1998 to 2002, he developed an interest in electrostatics and electromagnetics. In 2002, he joined The University of Manchester, Manchester, U.K., initially working in the area of electrical impedance tomography applied to industrial and medical problems and, more recently, in the area of electromagnetics. He has authored or coauthored more than 40 scientific publications. His current research interests include electromagnetic modeling, inverse problems, and magnetic induction sensor development.

Dr. Davidson received the Beloe Fellowship Award from the Worshipful Company of Scientific Instrument Makers in 2008.

David J. Daniels (Life Fellow, IEEE) led the development of radar for landmine detection, including programs for humanitarian demining in Lebanon, Cambodia, Bosnia, and Angola and for NATO forces in countering the threat from buried devices in Afghanistan. After a career in industry in applied research, in October 2014, he joined the School of Electrical and Electronic Engineering, The University of Manchester, Manchester, U.K., as a Visiting Professor. He has published over 110 technical articles and a number of books on sensing techniques for concealed objects, including *Ground Penetrating Radar* (Second Edition) and *EM Detection of Concealed Targets* as well as contributing to a number of seminal reference books in the field, including a contribution to *Radar Handbook* by Merrill Skolnik (Third Edition). His research and development interests are in sensors for security and counter terrorism in particular, short-range ultrawideband (UWB) radar, millimeter-wave, and submillimeter-wave radar systems.

Anthony J. Peyton received the B.Sc. degree in electrical engineering and electronics and the Ph.D. degree in medical instrumentation in 1983 and 1986, respectively, both from The University of Manchester Institute of Science and Technology (UMIST), Manchester, U.K.

After various positions in the scientific instrumentation industry and academia, he was appointed as a Professor in electromagnetic engineering in May 2004. He has over 30 years of experience in a diverse range of electromagnetic sensor systems and has been a Principal Investigator of numerous national, international, and industry-funded projects. He has coauthored over 150 international journal articles related to electromagnetics and sensing.